Chemical Engineering Journal Advances 28 (2026) 101426

Contents lists available at ScienceDirect

Chemical Engineering Journal Advances

journal homepage: www.sciencedirect.com/journal/chemical-engineering-journal-advances

Molecular dynamics investigation of structural and thermophysical properties of capric acid–silica nanocomposites under varying initial pressures

Narinderjit Singh Sawaran Singh [a], Mahmoud Fadhel Idan [b], Muthanna K. Kareem [c], Ibrahm Mahariq [d,e,*], Muntadher Abed Hussein [f], Albara Ibrahim Alrawashdeh [g,h], Laith S. Sabri [i], Mahmut Taner [j], Soheil Salahshour [k,l,m,n]

[a] Faculty of Data Science and Information Technology, INTI International University, Persiaran Perdana BBN, Putra Nilai, Nilai, 71800, Malaysia
[b] Department of Mechanical Power Techniques Engineering, College of Technical Engineering, University of Al Maarif, Al Anbar, 31001, Iraq
[c] College of Engineering, Al-Ayen University, Thi-Qar, Iraq
[d] University College, Korea University, Seoul, 02481, South Korea
[e] Department of Medical Research, China Medical University Hospital, China Medical University, Taichung, Taiwan
[f] University of Manara, Maysan, Iraq
[g] Department of General Subjects, College of Engineering, University of Business and Technology, Jeddah, 21361, Saudi Arabia
[h] Department of Chemistry and Chemical Technology, College of Science, Tafila Technical University, Tafila, 66110, Jordan
[i] College of Chemical Engineering, University of Technology- Iraq, Baghdad, 10066, Iraq
[j] Faculty of Engineering and Architecture, Istanbul Gelisim University, Istanbul, Türkiye
[k] Faculty of Engineering and Natural Sciences, Istanbul Okan University, Istanbul, Turkey
[l] Faculty of Engineering and Natural Sciences, Bahcesehir University, Istanbul, Turkey
[m] Research Center of Applied Mathematics, Khazar University, Baku, Azerbaijan
[n] Faculty of Science and Letters, Piri Reis University, Tuzla, Istanbul, Turkey

ARTICLE INFO

Keywords:
Molecular dynamics
Capric acid
Silica aerogel
Initial pressure
Energy Efficiency

ABSTRACT

The initial thermodynamic condition can influence the organizational behavior of molecules and the energy transportation in nanocomposites of phase change materials, whereas the pressure dependence property behavior of fatty acid-silica is not fully known on the molecular scale. In this work, MD simulations were performed to study the effects of the initial pressure of the first phase range of 1–3 bar, which impacts structural and thermo-physical properties for a capric acid-silica nanocomposite. The simulated system for the second-phase run was divided into two parts: first, an equilibration stage to maintain the system temperature at 300 K; second, a production stage to measure changes in local number density, atom velocity, temperature, heat flux, thermal conductivity, charging time, and discharging time. The consistency during thermal equilibration verified that the system reached a stable state, followed by evaluation. The maximum local number density at the heat reservoir increased from 0.0338 atoms/ to 0.0323 atoms/ under higher initial pressures, with a decrease in maximum velocities and temperatures from 0.0010 to 0.0008 Å/fs and 328.26 to 318.22 K. Concomitant decreases of thermal flux and thermal conductivity can also be observed during this period. The heat flux decreased from 8.10 to 7.79 W/m, and thermal conductivity from 0.29 to 0.23 W/mK, while the charge time slightly increased from 4.68 to 4.88 ns and the discharge time was almost invariant, close to the mean value of 6.19 ns, with slight variance at different initial pressures. In addition, this initial pressure can affect local molecular mobility and local structural properties. The research provides evidence of the influence of initial thermodynamic pressure on structural features, dynamics, and transport of the nanocomposite from a molecular view.

Abbreviations: TES, Thermal energy storage; PCM, Phase change material; TC, Thermal conductivity; MD, Molecular dynamics; SiA, Silica aerogel; Max-D, Maximum local number density; Max-V, Maximum velocity; NPs, Nanoparticles; Max-Temp, Maximum temperature; HF, Heat flux; PE, Potential energy; TE, Total energy; HT, Heat transfer; CT, Charging time; DT, Discharge time; P, Pressure.

* Corresponding author.
E-mail address: lbmmahariq@gmail.com (I. Mahariq).

https://doi.org/10.1016/j.ceja.2026.101426

Available online 18 August 2026

1. Introduction

With the growing requirement for optimized and sustainable energy utilization, enormous efforts have been devoted to researching thermal energy storage (TES) to cope with the fluctuating characteristics of intermittent energy, such as solar energy [1,2]. In parallel with advances in thermal storage, recent studies on nanostructured materials, including $Ce(OH)_3$-rGO nanocomposites, WS_2-loaded conductive polypyrrole matrices, and rare-earth high-entropy oxides, have demonstrated the important role of material design in improving electrochemical energy-storage performance [3,4]. For thermal applications, TES provides an effective approach for capturing and subsequently releasing thermal energy according to energy demand. Among the available TES approaches, latent heat storage using phase change materials (PCMs) is attractive because it combines relatively high energy-storage density with heat absorption and release over a narrow temperature (Temp) range [5–8]. Organic PCMs, particularly fatty acids, have received considerable attention because of their suitable phase-transition Temps, chemical stability, low toxicity, biodegradability, congruent melting, and relatively limited supercooling [9–11]. These characteristics make fatty acids promising materials for low- and moderate-Temp TES applications. However, their intrinsically low thermal conductivity (TC) and possible leakage during the liquid phase restrict heat-transfer rates and long-term practical performance [12,13].

As a result, combining organic PCMs with porous supporting matrices has already been shown to be a promising way to achieve shape-stabilized composites [14,15]. The characteristics of porous silica aerogels (SiAs) with low density, high porosity, large specific surface area, and an interconnected nanopore framework make them favored porous support materials [16,17]. By holding PCM, the porous silica framework can act as a physical barrier against bulk flow and alter the arrangement of molecules at the PCM-solid interface [18]. Thus, the thermal performance of these composites is determined not only by the intrinsic properties of PCM but also by other factors such as confinement effect, interface effect, and PCM's structural change inside or around the silica support, which are crucial for understanding their thermal stability and energy transportation performance [19,20].

In recent studies, we applied silica-based architectures and structures to stabilize organic PCM materials and alter their thermal properties. He et al [21] presented the application of alkylated SiAs encapsulating a paraffin mixture and incorporating wood fibers. They showed that nano-confinement and interfacial interactions of PCMs alter both melting and freezing transition behavior. Shen et al [22] prepared a paraffin/SiA composite that exhibited an adequate latent heat of 94.45 J/g with very little decay of enthalpy after 1000 freeze and thaw cycles. Silica-based encapsulation was investigated to enhance thermal stability and prevent leakage of PCMs. Chinnasamy et al [23] showed encapsulation of lauryl alcohol into a SiO-coated microcapsule. Encapsulated lauryl alcohol with a SiO shell yielded both melting and freezing latent heats of 90 and 88.2 J/g, respectively, whereas myristyl alcohol with a Hybrid Boron Nitride (h-BN)/Silica shell yielded higher heat-transfer performance [24]. Recently, more focus has been given to fatty-acid/silica-based PCMs. Liu et al [25] successfully encapsulated a capric acid-stearic acid mixture into nano-SiO shell-based microencapsulation. They reported improved thermal stability and prevented leakages with a high melting enthalpy of 138.16 J/g for an optimum formula, using additional expanded graphite (EG) and CuO to increase TC [26]. The preparation of capric acid-myristic acid-stearic acid/nano-SiO composite to control leakages and provide stability to the fatty acids mixture using physical confinement and capillarity was also achieved by Sun et al [27].

Due to these recent advances, silica-based encapsulation and supported structures have been extensively highlighted as an excellent approach for stabilizing leakages, structural stability, and transport phenomena in several review and experimental papers [28,29]. The molecular-level interactions that control phase-transition behaviors and transport phenomena through changes in molecular mobility, structure, and interfaces in fatty-acid/silica materials are still poorly addressed [30–32]. MD simulation has been increasingly applied to investigate phase transition characteristics and transport properties based on molecular motion, organization, and intermolecular interactions [30,31,33].

Although this improvement in PCM-in-matrix systems was made, prior research has typically emphasized measurements of macroscopic properties, including melting point, latent heat, TC, thermal resistivity, and cycling life of the composites. While providing fundamental information about the performance of composite materials, these measures gave little insight into the underlying molecular mechanisms that determined the structural assembly, molecular movement, and energy transmission at the PCM-silica interfaces. MD simulations played a crucial complementary role, allowing us to access atomic trajectories and intermolecular forces, thus enabling us to connect them to macroscopic thermal properties by tracking structural and dynamical changes occurring at the molecular and nanoscale [32,33]. This aspect would particularly apply to the fatty acids-based composite, in which intermolecular association at the interface greatly influences the transport properties.

An additional factor that received comparatively limited attention at the molecular scale was the initial thermodynamic state of the nanocomposite. In particular, the influence of initial pressure on capric acid–silica systems was not systematically resolved in terms of local number-density distribution, molecular mobility, Temp response, and thermal transport. Pressure can modify molecular spacing and intermolecular configurations, and the resulting equilibrated structure may subsequently influence energy transport. However, these effects could not be inferred reliably from macroscopic PCM measurements alone. A molecular-level assessment was therefore required to determine whether changes in the initial pressure state produced measurable differences in the subsequent structural and thermophysical response of the composite.

Hence, we used MD simulations to study a capric acid-silica nanocomposite under initial pressures from 1–3 bar. The organic phase PCM was capric acid because its phase change Temperature span matched the low Temperature range required for TES, whereas the inorganic silica phase offered a nanoscale solid surface, similar to real life, but in a pure form, with the latter being the solid supported by the real composite PEH. We chose a relatively small pressure range to examine how sensitive the composite was to small changes in its initial thermodynamic conditions, while changing nothing in terms of the material's composition under study. We examined the Maximum Local Number Density (Max-D), Maximum velocity (Max-V), maximum temperature (Max-T), heat flux (HF), TC, charging time (CT), and discharging time (DT). Instead of solely focusing on the final macroscopic indicator value and comparing across the tested material conditions and the pressure, the different parameters and such values were treated as molecular behavior- and structure-dependent variables that indicate, among other things, how their value changes under external compression and their dependence on different degrees of motion available to each atom/molecule. The primary achievement of the paper will therefore be to highlight how certain properties are very sensitive, while others are less dependent on the initial thermodynamic condition.

2. Molecular dynamics simulation

The initial molecular configurations were built in Avogadro, which was later used to pack them into the simulation box using Packmol. The initial cubic box size 150× 150× 150 $Å^3$ contained 75,780 atoms (See Fig. 1). The system size was chosen because it provided sufficient molecules around which the composite structures' behavior was to be evaluated, while not being too costly for 20 ns simulations. The application of periodic boundary conditions in all three Cartesian directions allowed us to model a bulk-like environment and prevent arbitrary free-

surface effects. The concentration of the additive was fixed to 1 at—% % for all considered systems. As we wanted to explore dependence on initial pressure without creating other independent parameter-additive concentration-we chose a relatively low, fixed percentage. Therefore, any dependence on pressure resulted from the dependence on initial state in a particular setting. Thus, all pressure-dependent simulations consisted of equally concentrated components and similarly sized cells. No wide sensitivity tests (for varying number of molecules and different concentration) were executed, since the task was to check the dependence only on the initial pressure in a fixed system and at constant composition. Therefore, the conclusions about pressure effects referred to the 150 150 150 box at fixed 1 at—% % additive. The initial temperature for all systems was 300 K. Before the equilibrium run, spheres closer than 0.5 were removed to prevent severe molecular overlaps. Energy was minimized using the conjugate-gradient method, and then atomic velocities were generated at 300K using an independent velocity seed. The time step was fixed to 0.1 fs during the entire run.

Thermal equilibration was subsequently conducted under the canonical ensemble using a Nose–Hoover thermostat at 300 K with a damping parameter of 10 fs. The equilibration stage was continued for 10 ns. After equilibration, the thermostat was removed, and the production stage was performed for an additional 10 ns. During production, fix nve was used for time integration together with a Berendsen barostat for pressure control. Separate simulations were conducted at target pressures of 1, 1.5, 2, 2.5, and 3 bar. Berendsen barostat continuously rescaled the simulation cell to relax the instantaneous pressure toward the prescribed target value. Each production simulation was continued for 10 ns. Three independent simulations were performed at each pressure using different initial velocity seeds, and the resulting properties were averaged, with the corresponding standard deviations reported as error bars. The complete simulation duration was therefore 20 ns. No thermostat was applied during the production stage to avoid direct thermostat interference with the energy and heat-flux fluctuations used for transport analysis. Structural, dynamical, and thermal quantities were extracted from the resulting production trajectories.

2.1. Force-field and interaction model

An atomistic, all-atom classical force-field description of molecular interactions was performed using the LAMMPS (Large-scale Atomic/Molecular Massively Parallel Simulator) simulation tool. Molecular structure assignment used in the additive was taken from [34], where "SiA", corresponding to PubChem CID 1151680, with a reported molecular formula of C23H22N2O3S2, was used. The molecular model had five types of atoms: C, H, N, O, and S. This molecular representation from the database was applied to all systems. Non-bonded interactions were represented by a combination of 12–6 Lennard-Jones (LJ) potential and pairwise Coulomb interactions. The LJ contribution was calculated as Eq. (1) [35]:

$$U_{LJ} = 4\varepsilon\left[\left(\frac{\sigma}{r}\right)^{12} - \left(\frac{\sigma}{r}\right)^{6}\right] r < r_c \tag{1}$$

where r is the separation between atoms i and j, ε represents the potential-well depth, and σ is the distance at which the LJ potential crosses zero. Electrostatic interactions between charged atoms were represented by Eq.(2):

$$U = \frac{Cq_iq_j}{\varepsilon_r r_{ij}} r_{ij} < r_c \tag{2}$$

where q_i and q_j are the partial atomic charges, and C is the unit-conversion factor associated with the real unit system. The non-bonded interactions were implemented using the lj/cut/coul/cut pair style. Cutoff distances of 10 Å and 8 Å were employed for the LJ and Coulomb contributions, respectively. Therefore, electrostatic interactions were evaluated as explicitly truncated pairwise Coulomb interactions, and no Ewald or particle–particle particle–mesh long-range electrostatic solver was employed. This interpretation follows directly from the selected LAMMPS pair style, for which two specified cutoff values correspond to the LJ and Coulomb cutoffs, respectively. The LJ parameters and partial atomic charges used in the simulations are summarized in Table 1.

Only the self-interaction LJ coefficients were explicitly specified in the input script. Consequently, the LJ coefficients for unlike atom pairs were generated using the default geometric mixing rule implemented in LAMMPS (Eqs. (3) and (4)) [36]:

$$\varepsilon_{ij} = \sqrt{\varepsilon_i \varepsilon_j} \tag{3}$$

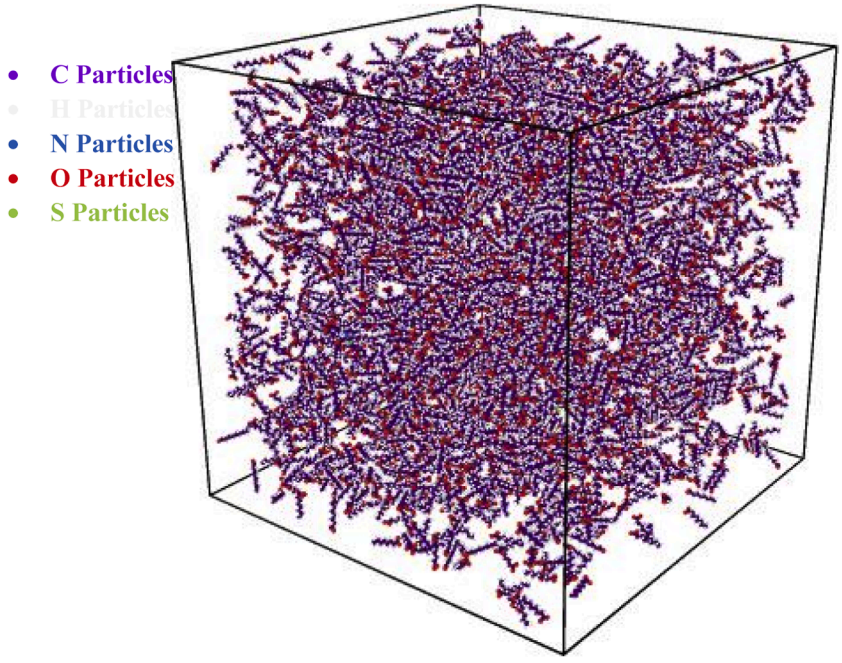

Fig. 1. Initial atomic configuration of the simulated capric acid–additive composite.

Table 1
Lennard-Jones parameters and partial atomic charges employed in the MD simulations.

Atom type	ε (kcal/mol)	σ (Å)	Charge (e)
C	0.305	3.725	−0.073
H	0.010	2.852	+0.049
N	0.415	3.561	−0.006
O	0.415	3.306	+0.007
S	0.215	3.690	+0.024

$$\sigma_{ij} = \frac{\sigma_i + \sigma_j}{2} \tag{4}$$

LAMMPS applies geometric mixing by default when unlike-pair coefficients have not been explicitly specified, and no alternative pair_modify mix setting is provided. Bond stretching and angle bending were represented using harmonic potentials (Eqs. (5) and (6)):

$$U_{bond} = K_b(r - r_0)^2 \tag{5}$$

$$U_{angle} = K_\theta(\theta - \theta_0)^2 \tag{6}$$

where K_b and K_θ denote the corresponding force constants, while r_0 and θ_0 represent the equilibrium bond length and angle, respectively; harmonic dihedral terms were additionally used to describe molecular torsional interactions. The complete bonded parameters employed in the simulations are summarized in Table 2.

The angle equilibrium values ranged from 92.10° to 109.471°, depending on the local atomic environment, while 18 dihedral types were included in the molecular topology. These bonded parameters were maintained unchanged for all pressure conditions so that differences between simulations could be attributed to the investigated initial thermodynamic state rather than changes in the interaction model.

2.2. Calculation of structural and thermophysical properties

The structural and thermophysical behavior of the system was analyzed by examining the local number density, local atomic velocity, and local temperature at specific points within the simulation box as well as the radial distribution function (RDF), HF, and TC as a whole. To resolve the spatially varying behaviors of the system, the simulation cell was binned into regions of width 1.5 in the x-direction. The local number density, y-component of atomic velocity, and local temperature were then time-averaged within each of these 1.5-wide spatial regions. The previous value referred to as Max-D should, more correctly, therefore be the maximum of the spatially binned number density profiles, rather than the mean number density for the whole of the simulation cell. This differentiation needs to be taken into account when looking at the dependence of Max-D on Pressure. The RDF, g_{ij} (r), was used to characterize the probability of finding atoms of type j at a distance r from atoms of type i relative to an ideal homogeneous distribution (Eq. (7)),

$$g_{ij}(r) = \frac{1}{4\pi r^2 \rho_j} \frac{dN_{ij}(r)}{dr} \tag{7}$$

where ρ_j is the number density of species j and $dN_{ij}(r)$ represents the number of atoms of type j within a spherical shell around species i. Pair-resolved RDF analysis was used to examine changes in local atomic organization under the investigated initial pressure conditions.

The microscopic heat-flux vector was calculated in LAMMPS from the per-atom kinetic energy, potential energy, and virial stress contributions using compute heat/flux. The instantaneous simulation volume normalized the heat-flux components. TC was subsequently evaluated using the equilibrium Green–Kubo formalism (Eq. (8)) [37].

$$K = \frac{V}{3k_B T^2} \int_0^\infty dt \langle J(\tau).J(0) \rangle \tag{8}$$

where k_B is the Boltzmann constant, T is the equilibrium temperature, V denotes the system volume, and J is the heat-current component

The heat-current autocorrelation functions along with x, y, and z directions were sampled using fix ave/correlate. In the implemented procedure, heat-current data were sampled every 100 timesteps, 10,000 correlation samples were considered, and the correlation output interval was 1.0×10^6 timesteps. Direction-dependent conductivity contributions were obtained by numerical integration of the corresponding heat-current autocorrelation functions.

The charging and DT were estimated by monitoring the time evolution of RDF in the thermal charging and discharging process. The RDF was traced as the molecular ordering and phase evolution descriptor. The DT, CT, was thus estimated to be the time when the RDF curve becomes equivalent to the characteristic stabilized distribution curve describing the structure of the thermally induced state from the attenuation of structural peaks appeared early in the transient time region and then saturation of RDF shape, while the DT, DT, was that in evolving towards the characteristic structure of the cooled state by sitting near equilibrium. Comparison could be directly performed at the same structure based on RDF among various CTs.

2.3. Equilibration assessment

The attainment of a proper equilibration state was evaluated based on the time dependence of T, PE, and TE in the NVT stage. Fig. 2 shows the evolution of PE at 300K. There was an initial fluctuation stage during which the molecular configuration relaxed energetically and structurally. After this fluctuation, the PE varied around a fixed mean, without a constant decrease over time (to 29.26kcal/mol), which means the primary energetic relaxation has been achieved. This equilibration did not

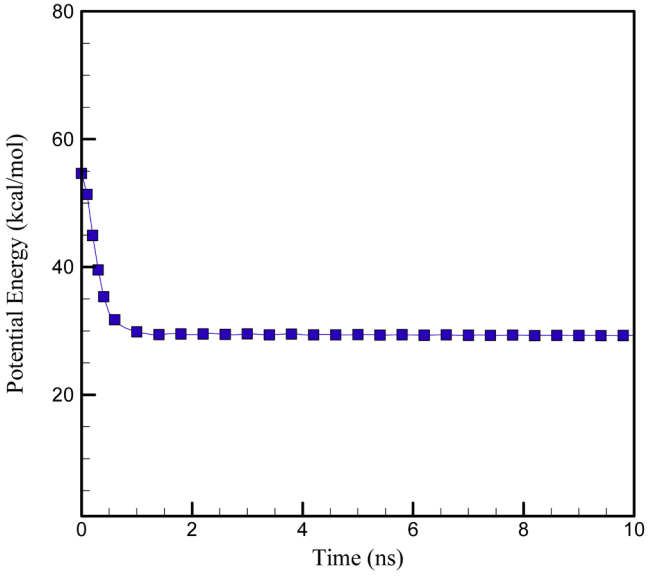

Fig. 2. Temporal evolution of the normalized potential energy during NVT equilibration at 300 K.

Table 2
Bond parameters employed in the molecular model.

Bond type	K_b (kcal/mol·Å²)	r_0 (Å)
C–C	350	1.530
C–H	350	1.090
C–N	350	1.462
C–O	350	1.420
C–S	350	1.800

mean that there existed an "average attractive force", as written in the original manuscript, but just that the energetic state of the system was quite stable under the NVT ensemble conditions.

Fig. 3 presents the corresponding evolution of TE, defined as the sum of PE and kinetic energy. Similar to PE, TE exhibited an initial transient followed by stationary fluctuations (to 30.18 kcal/mol). The simultaneous stabilization of Temp, PE, and TE was therefore used as the criterion for completing the 10 ns equilibration stage before initiating the NVE production calculations.

3. Radial distribution function

As an additional assessment of the structural characterization of the simulation systems, the RDF at 300 K was calculated following 10 ns equilibration. The RDF for pure capric acid at 300 K is depicted in Fig. 4a, and the RDF for the SiO-SiA nanocomposite is represented in Fig. 4b. RDF for pure capric acid, distinct short-range peaks were observed for the pure system with prominent peaks appearing near 1.2 and2.2Å, beyond approximately 3Å the intensity of RDF decreased significantly and only minor oscillations of RDF can be noticed beyond which no significant correlations were present in the short range scale. RDF profile changed quite noticeably upon addition of the silica-based additive, as shown in Fig. 4b. This nanocomposite showed a pronounced first peak near 1.1 Å and the following few oscillations that were observed between approximately 1.5 and 3.0 Å and at relatively larger ranges only a few oscillations were observed and that had a much lower amplitude, showing a clear change in the structure of pure capric acid as mentioned. These changes at shorter ranges were also compared with a well-characterized structure reported [38].

In addition to thermodynamic information about the behavior of the composite phase, the RDFs provided details concerning its structure. Strong short-range peaks and rapidly decaying longer-range correlations implied that the equilibrium structures of these systems had local ordering but no long-range positional order. By comparing the pure capric acid and nanocomposite RDFs, it is clear that the addition of the additive affected the organization of molecules at short range within the PCM. The relevance of these structural changes to what was happening molecularly during thermal energy storage was evident, and thus, in this work, they were used to describe the evolution of the structure with the charging and discharging processes. Nevertheless, this simulation was not set up to ascertain the detailed phase change thermodynamics of the nanocomposite, but rather to study the pressure dependence of molecular structure and thermal transport. Melting points, latent heats, specific heats, and long-term thermal cycling effects were not calculated. The calculation of such information would necessitate specifically designed heating/cooling simulations crossing the solid/liquid transition and running several cycling sequences. The information from the present work can thus only be considered an analysis on a molecular level.

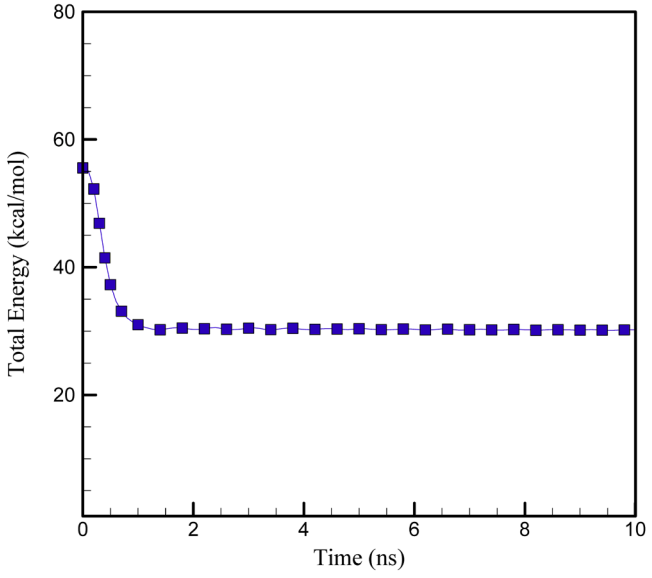

Fig. 3. Temporal evolution of the normalized total energy during NVT equilibration at 300 K.

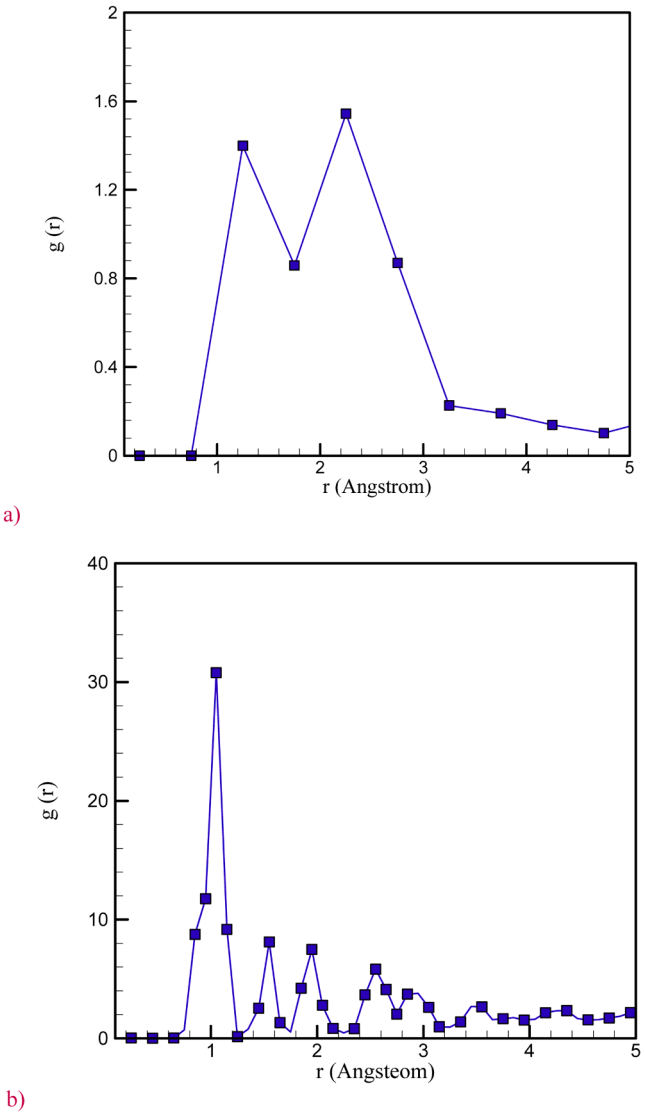

Fig. 4. RDFs of (a) pure capric acid and (b) the capric acid–SiA nanocomposite after 10 ns of equilibration at 300 K.

4. Results and discussion

Studies of pressure effects on the structural, dynamic, and thermal properties of capric acid-SiA composite material were performed at 1, 1.5, 2, 2.5 and 3 bar. Each study comprised three independent simulation runs, set up with a different initial seed in velocities and represented in the figure by error bars of statistical variations. Because several quantities studied below characterize local rather than bulk values of material (e.g., local or highest values of quantities considered), the dependence of properties on pressure will be explained in terms of variations in local density and local disorder.

The dependence of Max-D on Pressure is shown in Fig. 5. The value of Max-D decreased smoothly from 0.0338 atoms/ to 0.0323 atoms/ as the

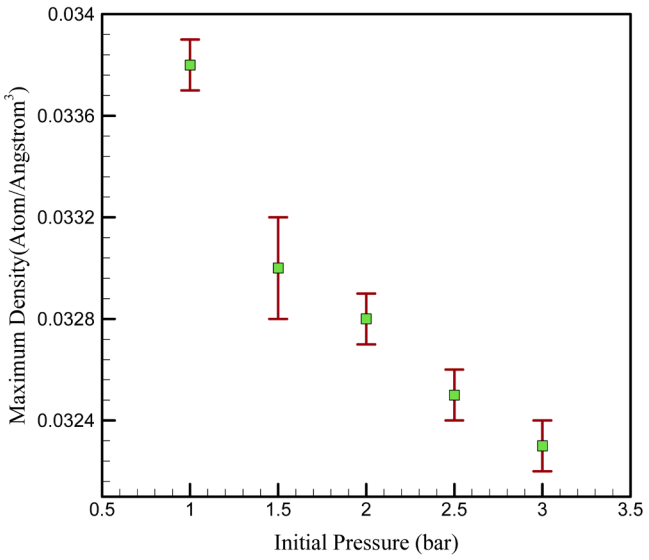

Fig. 5. Variation in the Max-D of the capric acid–SiA composite with pressure. Error bars represent the standard deviation obtained from three independent simulations.

pressure increased from 1 bar to 3 bar. The decrease in Max-D with Pressure can be attributed to a change in the atom configuration of space and to a decrease in the magnitude of the highest local densities.

As the distance between atoms and the short-range forces were modified due to increased pressure, the atoms were reorganized and redistributed. The atomic distribution was not localized in the maximum crowded area but rather distributed more evenly across the whole system, thus reducing Max-D. Similarly, a decrease in the value of Max-D with increasing pressure was observed for the paraffin/copper system [39], where increasing pressure reduced the maximum local density. The error bars obtained from three independent simulations confirm the reproducibility of the observed pressure-dependent trend.

Fig. 6 shows the atomic behavior of the nanocomposite, exhibiting velocity distribution at 1 bar (Fig. 6a) and pressure dependence of Max-V (Fig. 6b). Atomic velocities had a dispersed distribution at 1 bar. There was no single, constant Max-V (Fig. 6a), demonstrating that the molecular behavior was heterogeneous. Atoms concentrated on the lower to moderate velocity ranges, and the high-velocity events were only distributed in the tail of atomic velocity distributions. From Fig. 6b, it can be noted that the average Max-V reduced approximately from 0.0010 Å/fs at 1 bar to 0.0008 Å/fs at 3 bar, (i.e., about 100m/s to 80m/s), owing to the effect of pressure to molecular neighborhood on which atoms underwent shorter-range collision as free volumes and molecular spaces being minimized at increasing pressures, leading to increased interactions among different species and Pressure driven structural/reorganizational effects restricting translational motion. Numerical results of Max-D, Max-v, and Max-temp at different pressures are given in Table 3.

Fig. 7 shows that the trend of Max-Temp with initial pressure varied from 328.26 K at 1 bar to 318.22 K at 3 bar. This implies that as the initial pressure increased, the values of local largest thermal fluctuations became lower in the case of the composite. The rationale behind this trend was that increased pressure changed the degree of free volume for molecular mobility and redistribution of kinetic energy among neighboring molecules. For example, with the higher pressure values the number of intermolecular interactions at close range increased, and at the same time the mobility volume available became smaller due to restriction of large molecular scale motion of molecules so energy redistributed for maximum number of neighbors to share minimum amounts energy with others, which in turn made the occurrence of individual maximum kinetic-energy localization low and the resulting

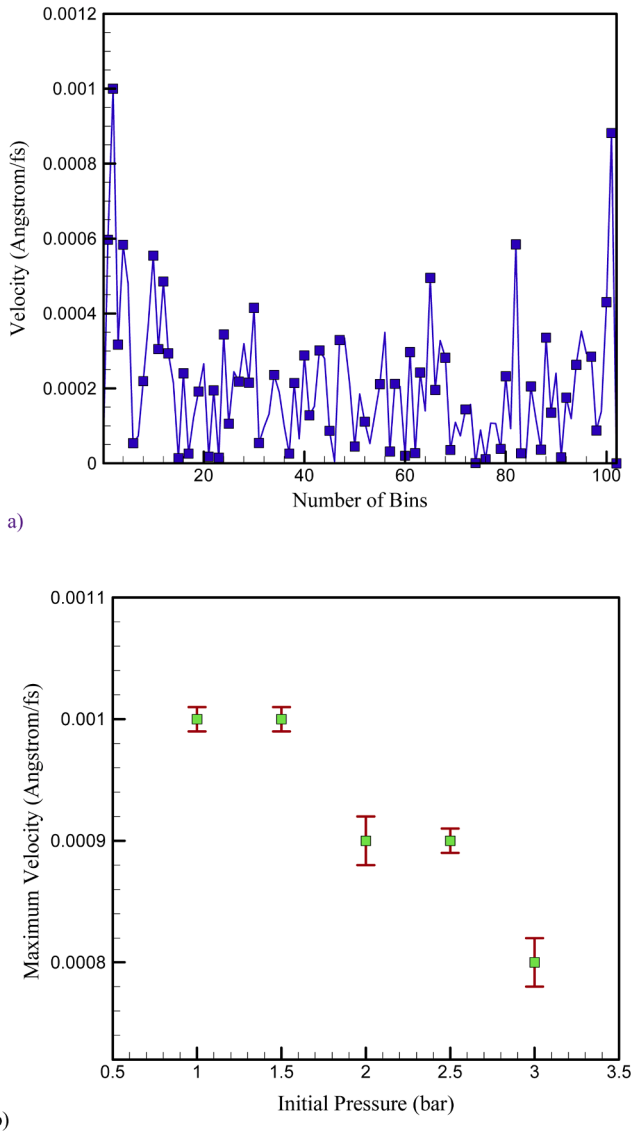

Fig. 6. Atomic velocity characteristics of the capric acid–SiA nanocomposite: (a) atomic velocity distribution at an initial pressure of 1 bar and (b) variation in Max-V with initial pressure. Error bars in (b) represent the standard deviation of three independent simulations.

Table 3
Numerical results of Max-D, Max-v, and Max-temp at different pressures.

Initial pressure (bar)	Max-D (atom/Å^3)	Max-V (Å / fs)	Max-Temp (K)
1	0.0338 (±0.0001)	0.001 (±0.00001)	328.26 (±0.52)
1.5	0.033 (±0.0002)	0.001 (±0.00001)	325.15 (±0.91)
2	0.0328 (±0.0001)	0.0009 (±0.00002)	320.91 (±0.63)
2.5	0.0325 (±0.0001)	0.0009 (±0.00001)	319.14 (±0.52)
3	0.0323 (±0.0001)	0.0008 (±0.00002)	318.22 (±0.88)

local highest Temp would be reduced. The result was in agreement with the Max-V as discussed above in Fig. 6, that with the increment of the initial Pressure, Max-V also declined. This type of reduction of Temp versus initial pressure was found in the works of Gao et al [40] in SiA / PCM / CuO nanostructure; the range of highest Temp was from 931.42 K reduced to 895.63 K by raising the initial pressures, which agreed well with this study finding that high pressure can limit the motion of molecules and reduce the highest localized Temp among neighbors for silica-aerogel / PCM based TES system. Three individual runs with error bars confirmed that this tendency was repeatable.

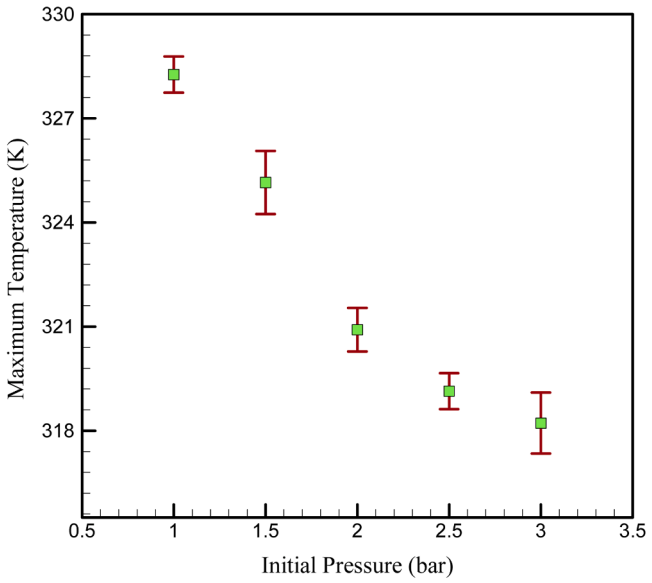

Fig. 7. Variation in the Max-Temp of the capric acid–SiA composite with initial pressure. Error bars represent the standard deviation of three independent simulations.

Fig. 8 plots the dependence of the HF on the initial pressure. It shows a decline of HF with initial pressure from 8.10 W/m at 1 bar to 7.79 W/m at 3 bar. This means the microscopic energy transfer weakened as pressure increased. One reason for this decrease could be the compression-induced effect on molecular structure (packing) and mobility. The microscopic motions contributed 73.74 W/m to thermal transport at 1 bar and 70.88 W/m at 3 bar. As pressure increased, the available free volume reduced, and intermolecular interactions among atoms became more important. Short-range interactions more easily led to the redistribution of energy between nearby atoms and a decrease in large-amplitude motion of atoms. This, in turn, may weaken the extent and lifetime of high-mobility, high-energy microscopic energy currents. The reduction of both Max-V and Max-Temp provided supporting evidence for this description at initially increased pressure. The calculated HF value decreased with increasing initial pressure. Thus, the averaged result of three independent simulations (shown with error bars) showed good agreement with each other and represented a stable decrease in HF.

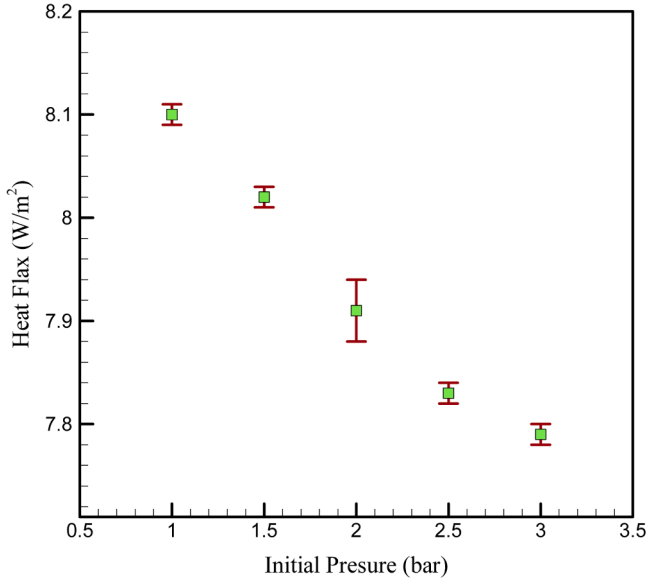

Fig. 8. Variation in the HF of the capric acid–SiA composite with initial pressure. Error bars represent the standard deviation of three independent simulations.

Before studying the pressure dependence of TC, Green-Kubo was checked for convergence by taking measurements of HCACF, presented as HCACF versus correlation number in Fig. 9. HCACF quickly decreased at lower numbers of correlations and then fluttered around the baseline, damping out more, and the ACACF oscillated around zero after a significant increase in the number of correlations. This decrease and loss of continued oscillation at low correlation means that the size of correlations was large enough to use for green-kubo integration; the result was insensitive to running the HCACF for longer.

Fig. 10 shows the change in TC versus initial pressure. As the pressure increased from 1 to 3 bar, the average TC went from 0.29 to 0.23 W/mK, showing that the composite was less adept at carrying thermal energy. This may be understood by considering the effects of pressure on molecular structure and dynamics of energy transfer. When the pressure increased, the available free volume decreased, and more high-energy short-range molecular interactions hindered molecular mobility and changed the nature of the channels through which fluctuations in energy were transferred between neighboring atoms and molecules. In turn, this led to smaller amplitude and shorter lifetime of correlated microscopic heat-current fluctuations, thus a lower Green-Kubo TC. This interpretation was consistent with the corresponding declines in HF, Max-V, and Max-Temp, all indicating less molecular mobility and microscopic energy transport at high pressure. The error bars from three runs ensured that the decreasing trend observed overall was indeed reliable.

Fig. 11 presents the variation in CT with initial pressure. Increasing the pressure from 1 to 3 bar increased the mean CT from 4.68 to 4.88 ns, indicating that the structural evolution associated with the charging process became slightly slower at higher pressure. This means that structural relaxation related to the charging process became slightly slower at higher pressure. The higher pressure means that molecular motion was being restrained to some extent due to the effect of pressure. That is, the free volume space and short-range intermolecular interactions became denser as pressure increased, and the mobility of molecules was inhibited. Capric acid molecules spent more time reaching the stabilized configuration predicted from the RDF, as their rearrangement was prevented; the time to stabilize the profile was longer, and CT increased accordingly. This trend of CT increase matched the decreases in Max-V, HF, and TC, all indicating reduced molecular mobility and microscopic energy-transport kinetics under higher

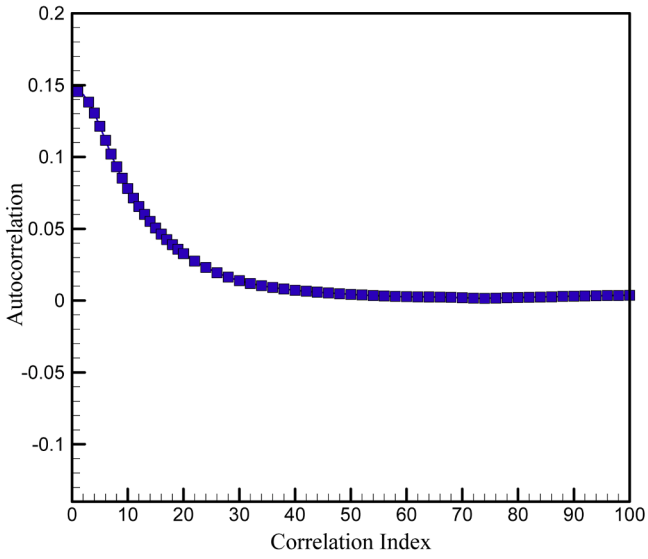

Fig. 9. HCACF as a function of correlation index used to evaluate the convergence of the Green–Kubo calculation.

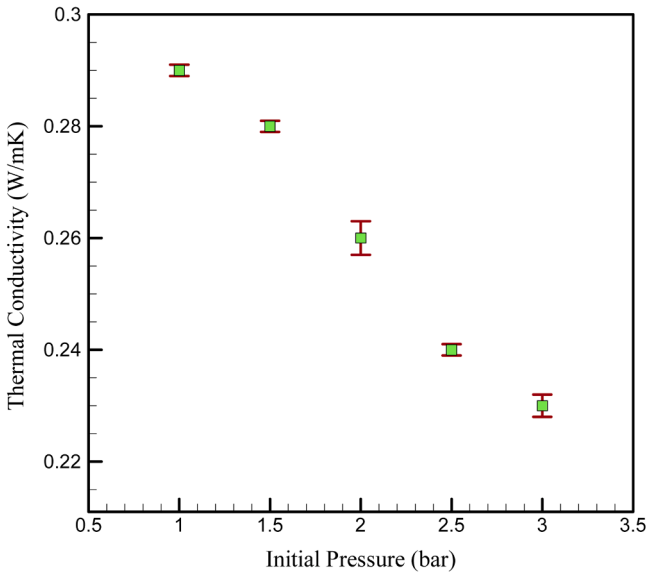

Fig. 10. Variation in the TC of the capric acid–SiA composite with initial pressure. Error bars represent the standard deviation of three independent simulations.

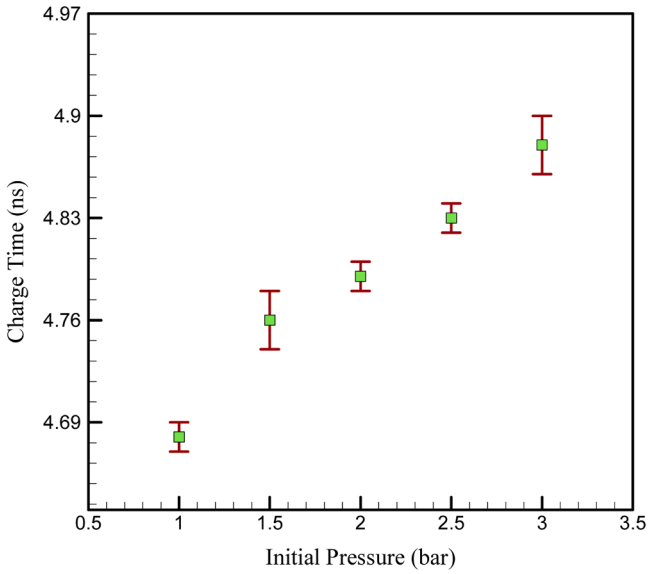

Fig. 11. Variation in the CT of the capric acid–SiA composite with initial pressure. Error bars represent the standard deviation of three independent simulations.

pressure. The accuracy of these trends was proven by the reproducibility obtained after three runs each time.

Fig. 12 shows the behavior of DT against initial pressure. This contrasts with the behavior of CT at increasing initial pressure. It varied only slightly and in a non-monotonic fashion within the measured pressure range. Increasing the pressure from 1 to 2 bar caused a very small reduction in the mean DT from 6.19 to 6.18 ns. Raising the pressure to 2.5 bar yielded a slight increase to 6.20 ns, then a reduction again back to around 6.19 ns at 3 bar. This varied by only 0.01-0.02 ns, indicating that pressure played a small role in the structural relaxation that occurred as part of discharge. The structure became more ordered with less energy on discharging, so this implied that this RDF-based restructuring took place at the same speed over the measured pressure range. Furthermore, the overlap between the error bars means the difference among adjacent points was simply statistical error from

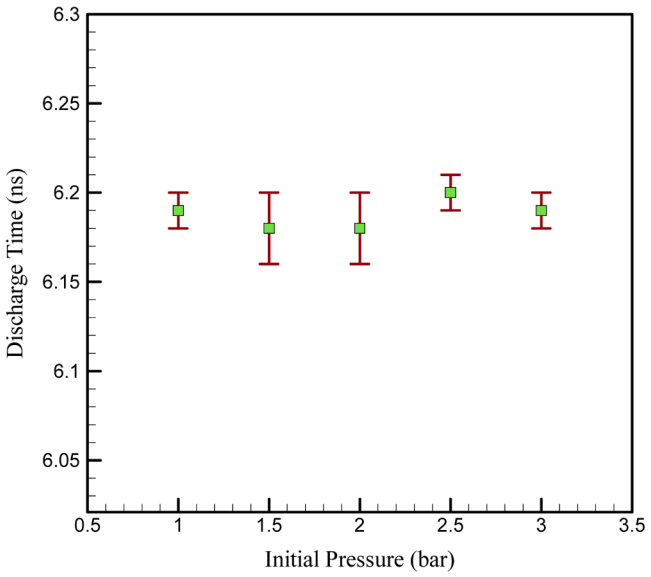

Fig. 12. Variation in the DT of the capric acid–SiA composite with initial pressure. Error bars represent the standard deviation of three independent simulations.

independent simulations. There was no trend, so it can be observed that the discharge behavior was fairly constant between 1 and 3 bar. Numerical results of TC, HF, CT, and DT at different pressures are given in Table 4.

5. Conclusion

A Molecular Dynamics simulation was conducted to probe the effects of initial pressure on the structural and thermophysical characteristics of capric acid-silica nanocomposites. Both equilibration and production simulations were run for 10 ns each. Equilibration was monitored by the stabilization of potential and total energies, and the effects of three different initial pressures were observed through maximum local number density (Max-D), maximum atomic velocity (Max-V), maximum Temp (Max-Temp), heat flux (HF), thermal conductivity (TC), charging time (CT), and discharging time (DT). Three different simulations were conducted, and the pressure-dependent trends were analyzed using three different initial velocity seeds. The main findings are summarized as follows:

- The potential energy converged to approximately 29.26 kcal/mol after 10 ns, with stationary fluctuations indicating that the system reached an energetically equilibrated state.
- The total energy stabilized at approximately 30.18 kcal/mol after 10 ns, further confirming the establishment of a stable equilibrium condition before the subsequent pressure-dependent analysis.

Table 4
Numerical results of TC, HF, CT, and DT at different pressures.

Initial pressure (bar)	HF (W/m^2)	TC (W/m.K)	CT (ns)	DT (ns)
1	8.1 (±0.01)	0.29 (±0.001)	4.68 (±0.01)	6.19 (±0.01)
1.5	8.02 (±0.01)	0.28 (±0.001)	4.76 (±0.02)	6.18 (±0.02)
2	7.91 (±0.03)	0.26 (±0.003)	4.79 (±0.01)	6.18 (±0.02)
2.5	7.83 (±0.01)	0.24 (±0.001)	4.83 (±0.01)	6.20 (±0.01)
3	7.79 (±0.01)	0.23 (±0.002)	4.88 (±0.02)	6.19 (±0.01)

- Max-D decreased from 0.0338 to 0.0323 atoms/Å^3 as pressure increased from 1 to 3 bar, indicating pressure-induced redistribution of atoms and a reduction in the highest local density regions rather than a decrease in the bulk density of the entire system.
- Max-V decreased from 0.0010 to 0.0008 Å/fs as Pressure increased from 1 to 3 bar. The reduced maximum velocity was associated with decreased free volume, more frequent short-range interactions, and greater momentum redistribution among neighboring atoms.
- Max-T decreased from 328.26 to 318.22 K with increasing pressure, indicating suppression of the highest local thermal fluctuations and reduced large-amplitude molecular motion.
- HF decreased from 8.10 to 7.79 W/m^2 as Pressure increased from 1 to 3 bar, demonstrating that pressure-induced changes in molecular organization and mobility reduced microscopic energy transport.
- TC decreased from 0.29 to 0.23 W/m·K over the investigated pressure range, consistent with changes in molecular organization and reduced magnitude and persistence of correlated microscopic heat-current fluctuations.
- CT increased from 4.68 to 4.88 ns as pressure increased from 1 to 3 bar. The RDF-based analysis indicated that reduced molecular mobility at higher pressure slowed the structural rearrangement required to reach the stabilized thermally evolved configuration.
- DT remained nearly unchanged, varying only between approximately 6.18 and 6.20 ns. Considering the small differences and associated statistical uncertainty, no systematic pressure-dependent trend was identified for the discharging process.

In summary, increased initial pressure primarily altered the local structure, molecular mobility, and microscopic heat transport of the capric acid-silica nanocomposite, yielding smaller values of Max-D, Max-V, Max-T, HF, TC, and a small increase in CT, while the DT was relatively insensitive to pressure in the 1-3 bar range considered. Our observations suggest that the response to pressure varies for different properties and provide insight at the molecular level, aiding the design and operational environment of silica-supported PCM for energy storage.

CRediT authorship contribution statement

Narinderjit Singh Sawaran Singh: Conceptualization, Methodology, Software, Validation, Formal analysis, Investigation, Resources, Data curation. **Mahmoud Fadhel Idan:** Visualization, Supervision, Project administration, Funding acquisition. **Muthanna K. Kareem:** Writing – original draft, Writing – review & editing. **Ibrahm Mahariq:** Writing – original draft, Writing – review & editing. **Muntadher Abed Hussein:** Conceptualization, Methodology, Software, Validation, Formal analysis. **Albara Ibrahim Alrawashdeh:** Supervision, Project administration, Funding acquisition. **Laith S. Sabri:** Formal analysis, Investigation, Resources, Data curation, Writing – original draft, Writing – review & editing, Visualization. **Mahmut Taner:** Writing – original draft, Writing – review & editing, Visualization, Supervision, Project administration, Funding acquisition. **Soheil Salahshour:** Conceptualization, Methodology, Software, Validation, Formal analysis, Investigation, Resources, Data curation, Writing – original draft.

Declaration of competing interest

The authors declare that they have no known competing financial interests or personal relationships that could have appeared to influence the work reported in this paper.

Data availability

No data was used for the research described in the article.

References

[1] M. Semadeni, Energy storage as an essential part of sustainable energy systems: a review on applied energy storage technologies, CEPE Work. Pap. 24 (2003), https://doi.org/10.3929/ethz-a-004532521.

[2] H.P. Garg, S.C. Mullick, V.K. Bhargava, Solar thermal energy storage, Springer Science & Business Media, 2012 9789400953017. ISBN:9400953011.

[3] R. Islam, R.S. Ballal, P.E. Lokhande, S. Katavkar, D. Lokhande, H. Mudila, S. Khasim, et al., Strategic WS2 loading in conductive polypyrrole matrices for next-generation supercapacitors, Mater. Chem. Phys. (2026) 132697, https://doi.org/10.1016/j.matchemphys.2026.132697.

[4] P.E. Lokhande, R.S. Ballal, D. Mohite, V. Kadam, S. Khasim, A. Almasoudi, R. Aepuru, U. Rednam, Facile microwave-assisted synthesis of Ce (OH) 3-rGO nanocomposites for high-performance supercapacitor applications, J. Rare Earths (2026), https://doi.org/10.1016/j.jre.2026.07.017.

[5] Denholm, P., E. Ela, B. Kirby, and M. Milligan. "The role of energy storage with renewable electricity generation." (2010): 1. Technical Report NREL/TP-6A2-47187 January 2010 https://oasis.library.unlv.edu/renew_pubs/5.

[6] I. Sarbu, C. Sebarchievici, A comprehensive review of thermal energy storage, Sustainability 10 (no. 1) (2018) 191, https://doi.org/10.3390/su10010191.

[7] B. Zalba, J. Ma Marín, L.F. Cabeza, H. Mehling, Review on thermal energy storage with phase change: materials, heat transfer analysis and applications, Appl. Therm. Eng. 23 (no. 3) (2003) 251–283, https://doi.org/10.1016/S1359-4311(02)00192-8.

[8] Muruganantham, K. "Application of phase change material in buildings: field data vs. EnergyPlus simulation," (2010) Arizona State University ProQuest Dissertations & Theses, 2010. 1483354. https://ui.adsabs.harvard.edu/abs/2010PhDT.....211M.

[9] P. Herrera, H. De la Hoz Siegler, M. Clarke, Fatty acids as phase change materials for building applications: drawbacks and future developments, Energies 17 (no. 19) (2024) 4880, https://doi.org/10.3390/en17194880.

[10] A. Anand, K. Kant, A. Shukla, C.-R. Chen, A. Sharma, Thermal stability and reliability test of some saturated fatty acids for low and medium temperature thermal energy storage, Energies 14 (no. 15) (2021) 4509, https://doi.org/10.3390/en14154509.

[11] M. Duquesne, C. Mailhé, S. Doppiu, J.-L. Dauvergne, S. Santos-Moreno, A. Godin, G. Fleury, F. Rouault, E.P. del Barrio, Characterization of fatty acids as biobased organic materials for latent heat storage, Materials 14 (no. 16) (2021) 4707, https://doi.org/10.3390/ma14164707.

[12] D. Rozanna, T.G. Chuah, A. Salmiah, T.S.Y. Choong, M. Sa'Ari, Fatty acids as phase change materials (PCMs) for thermal energy storage: a review, Int. J. Green Energy 1 (no. 4) (2005) 495–513, https://doi.org/10.1081/GE-200038722.

[13] Y. Yuan, N. Zhang, W. Tao, C. Xiaoling, H. Yaling, Fatty acids as phase change materials: a review, Renew. Sustain. Energy Rev. 29 (2014) 482–498, https://doi.org/10.1016/j.rser.2013.08.107.

[14] A. Sharma, V. Veer Tyagi, C.R. Chen, D. Buddhi, Review on thermal energy storage with phase change materials and applications, Renew. Sustain. Energy Rev. 13 (no. 2) (2009) 318–345, https://doi.org/10.1016/j.rser.2007.10.005.

[15] M.F. Demirbas, Thermal energy storage and phase change materials: an overview, Energy Sources B: Econ. Plan. Policy 1 (no. 1) (2006) 85–95, https://doi.org/10.1080/009083190881481.

[16] X. Huang, Z. Liu, W. Xia, R. Zou, R.P.S. Han, Alkylated phase change composites for thermal energy storage based on surface-modified silica aerogels, J. Mater. Chem. A 3 (no. 5) (2015) 1935–1940, https://doi.org/10.1039/c4ta06735e.

[17] P. Liu, X. Chen, Y. Li, P. Cheng, Z. Tang, J. Lv, W. Aftab, G. Wang, Aerogels meet phase change materials: fundamentals, advances, and beyond, ACS Nano 16 (no. 10) (2022) 15586–15626, https://doi.org/10.1021/acsnano.2c05067.

[18] M. Zhang, Q. Xiao, C. Chen, L. Li, W. Yuan, Developing a heat-insulating composite phase change material with light-to-thermal conversion performance from graphene oxide/silica hybrid aerogel, Appl. Therm. Eng. 174 (2020) 115303, https://doi.org/10.1016/j.applthermaleng.2020.115303.

[19] L. Jiang, X. Hu, G. Yi, S. Xiao, Y.Q. Xie, B. Chen, J. Wang, et al., Effects of carbonization temperature on the thermal characteristics of shape-stable composite phase change materials based on silica aerogel, J. Energy Storage 72 (2023) 108457, https://doi.org/10.1016/j.est.2023.108457.

[20] P. Liu, H. Gao, X. Chen, D. Chen, J. Lv, M. Han, P. Cheng, G. Wang, In situ one-step construction of monolithic silica aerogel-based composite phase change materials for thermal protection, Compos. B: Eng. 195 (2020) 108072, https://doi.org/10.1016/j.compositesb.2020.108072.

[21] L. He, K. Ling, M. Wang, X. Zhang, J. Li, Y. Chen, Y. Fan, Improving the phase change properties of paraffin wax by regulating the pore structure and surface properties of silica aerogel, J. Energy Storage 83 (2024) 110665, https://doi.org/10.1016/j.est.2024.110665.

[22] L. Shen, H. Tan, Y. Yang, W. He, Preparation and characteristics of paraffin/silica aerogel composite phase-change materials and their application to cement, Constr. Build. Mater. 387 (2023) 131609, https://doi.org/10.1016/j.conbuildmat.2023.131609.

[23] V. Chinnasamy, N. You, H. Cho, Development and thermophysical investigation of stable fatty alcohol/SiO2 phase change material microcapsules through interfacial polycondensation, J. Mater. Res. 39 (no. 19) (2024) 2696–2706, https://doi.org/10.1557/s43578-024-01417-2.

[24] V.S. Reddy, S. Venkatachalapathy, P.V.R. Nanda Kishore, Study on thermal performance and flow behavior of myristyl alcohol phase change material microencapsulated with hybrid shell in minichannels, Appl. Therm. Eng. 257 (2024) 124138, https://doi.org/10.1016/j.applthermaleng.2024.124138.

[25] L.I.U. Fengli, L.I. Qiaoli, B.A.I. Jianxia, W. Yaguang, Preparation and performance optimization of CA-SA@SiO2 microencapsulated phase change materials for construction, J. Funct. Mater. 55 (8) (2024) 8096–8102, https://doi.org/10.3969/j.issn.1001-9731.2024.08.013.
[26] S. Yin, M. Lu, C. Liu, L. Tong, L. Wang, Y. Ding, Fabrication and thermal properties of capric–stearic acid eutectic/nano-SiO2 phase change material with expanded graphite and CuO for thermal energy storage, J. Energy Storage 77 (2024) 110025, https://doi.org/10.1016/j.est.2023.110025.
[27] Y. Sun, F. He, J. Wang, L. Wang, B. Fu, W. Tang, Preparation and characterization of fatty acid ternary eutectic mixture/Nano-SiO2 composite phase change material for building applications, Appl. Energy 376 (2024) 124221, https://doi.org/10.1016/j.apenergy.2024.124221.
[28] K. Mishra, S. Singh, R. Agarwal, N. Babu Balam, R. Kumar, B.S. Naik, Silica-based microencapsulation of phase change materials for efficient thermal energy storage: a comprehensive review, Energy Storage 7 (no. 4) (2025) e70189, https://doi.org/10.1002/est2.70189.
[29] G. Wang, L. Liu, X. Hu, P. Hu, M. Li, X. Zhang, J. Wang, Aerogel-functionalized phase change materials toward lightweight and robust thermal management, Small Methods 9 (no. 8) (2025) 2500127, https://doi.org/10.1002/smtd.202500127.
[30] H. Hassanloo, X. Wang, Y. Yang, Characterising phase transition and thermal behaviour of phase change material with nanobubbles: a comparative molecular dynamics study, Int. Commun. Heat Mass Transf. 171 (2026) 110113, https://doi.org/10.1016/j.icheatmasstransfer.2025.110113.
[31] M. Yari, D. Toghraie, M. Riyahi, R. Kalbasi, M. Haratian, Investigation of temperature-dependent structural and thermal behavior in capric acid–silica nanocomposites via molecular dynamics simulation, J. Eng. Res. (2026), https://doi.org/10.1016/j.jer.2026.06.007.
[32] J. Kim, Y. Liu, T. Luo, Z. Tian, Molecular dynamics simulations in nanoscale heat transfer: a mini review, ASME J. Heat Mass Transf. 147 (no. 3) (2025) 030801, https://doi.org/10.1115/1.4067341.
[33] Y. Ran, V. Bertola, Achievements and prospects of molecular dynamics simulations in thermofluid sciences, Energies 17 (no. 4) (2024) 888, https://doi.org/10.3390/en17040888.
[34] National Center for Biotechnology Information. PubChem Compound summary for CID 1151680, Silica aerogel. https://pubchem.ncbi.nlm.nih.gov/compound/1151680. Accessed August 8, 2026.
[35] J.E. Lennard-Jones, Cohesion, Proc. Phys. Soc. 43 (no. 5) (1931) 461–482, https://doi.org/10.1088/0959-5309/43/5/301.
[36] H.J.C. Berendsen, J.-R. Grigera, T.P. Straatsma, The missing term in effective pair potentials, J. Phys. Chem. 91 (no. 24) (1987) 6269–6271, https://doi.org/10.1021/j100308a038.
[37] M.S. Green, Markoff random processes and the statistical mechanics of time-dependent phenomena. II. Irreversible processes in fluids, J. Chem. Phys. 22 (no. 3) (1954) 398–413, https://doi.org/10.1063/1.1740082.
[38] National Center for Biotechnology Information, PubChem compound summary for CID 2969, Decanoic Acid (2026). Retrieved August 9, 2026 from, https://pubchem.ncbi.nlm.nih.gov/compound/Decanoic-Acid.
[39] D.J. Jasim, A.B.M. Ali, A.H. Ali, S. Salahshour, S. Esmaeili, The effect of initial pressure and temperature on the flow in a three-dimensional cavity filled with paraffin/Cu nanostructure with a wavy lower wall and a movable upper wall using molecular dynamics simulation, Int. J. Thermofluids 24 (2024) 100862, https://doi.org/10.1016/j.ijft.2024.100862.
[40] Y. Gao, A. Basem, S.M. Sajadi, D.J. Jasim, N. Nasajpour-Esfahani, S. Salahshour, S. Esmaeili, S. Baghaei, The effect of initial pressure on the thermal behavior of the silica aerogel/PCM/CuO nanostructure inside a cylindrical duct using molecular dynamics simulation, Case Stud. Therm. Eng. 54 (2024) 104064, https://doi.org/10.1016/j.csite.2024.104064.